Supplement of Atmos. Chem. Phys., 21, 9105–9124, 2021
https://doi.org/10.5194/acp-21-9105-2021-supplement
© Author(s) 2021. CC BY 4.0 License.

Supplement of

Large-scale synoptic drivers of co-occurring summertime ozone and $PM_{2.5}$ pollution in eastern China

Lian Zong et al.

Correspondence to: Yuanjian Yang (yyj1985@nuist.edu.cn)

The copyright of individual parts of the supplement might differ from the article licence.

Text S1-S3

Text S1. The calculation on BLH according to Seidel et al. (2012) and Guo et al. (2016, 2019).

The bulk Richardson number (*Ri*) was applied to calculate the BLH.

Ri is expressed as:

$$R(i) = \frac{(g/\theta_{vs})(\theta_{vz}-\theta_{vs})(z-z_s)}{(u_z-u_s)^2+(v_z-u_s)^2+(bu_*^2)} \quad (1)$$

where *z* is height above ground, *s* is the surface, g is the acceleration due to gravity, θ_v is virtual potential temperature, u and *v* are the component of wind speed, and u_* is the surface friction velocity. Due to a smaller magnitude in compared with bulk wind shear term in the denominator, this study does not need to consider the influence of u_* (Seidel et al., 2012).

Text S2. Determining the number of synoptic patterns.

The explained cluster variance (ECV) ranging from 0 to 1is selected to assess the performance of synoptic classification and to determine the number of classes (Hoffmann & SchlüNzen, 2013; Philipp et al., 2014). ECV is defined as**:**

$$ECV = 1 - \frac{WS}{TS} \tag{2}$$

Where *WS* is the sum of squares within synoptic patterns, and *TS* is the total of sum of squares:

$$WS = \sum_{j=1}^{k} \sum_{i \in C_j} D^2{}_{(Y_i, \overline{Y_j})} \tag{3}$$

$$TS = \sum_{i=1}^{n} \sum_{l=1}^{m} (Y_{il}, \overline{Y_l})^2 \tag{4}$$

where k is synoptic patterns number, C_j is the pattern j, and the squared Euclidean distance $D^2{}_{(Y_i, \overline{Y_j})}$ between an element and its centroid is defined as:

$$D^2{}_{(Y_i, \overline{Y_j})} = \sum_{l=1}^{m} \left(Y_{il}, \overline{Y_{jl}}\right)^2 \tag{5}$$

where l is the time step (l=1, 2, …, m), Y_{il} is the respective data point, $\overline{Y_{jl}}$ is the estimate of the mean value for synoptic pattern j, $\overline{Y_l}$ is the estimate of the total mean.

Then, the synoptic patterns number k can be determined by the increment of the *ECV* value (Ning et al., 2019):

$$\Delta ECV = ECV_k - ECV_{k-1} \tag{6}$$

An important criterion to determine the number of SWPs is to ensure that the differences between different synoptic patterns are the largest, while the differences within the same synoptic pattern is the smallest. ECV is usually recommended as an indication, as a greater ECV value often corresponds to a better performance of the synoptic pattern classification (Hoffmann and Heinke SchlüNzen, 2013). The highest value of ΔECV means that the performance in the synoptic pattern classification is improved substantially (Ning et al., 2019). Therefore, both higher ECV and ΔECV values were considered in our study. We found the small value of ECV when the number of SWPs was two or three, indicating greater differences within the same synoptic pattern. The ECV value showed the highest increase when the number of SWPs was four, which means the differences within the same synoptic pattern was significantly improved (Fig. S1). Therefore, four SWPs were finally selected in our study.

Text S3. The consistencies between the NCEP data and ERA-5 data.

For further analysis of the modulation of the co-occurrence of O_3–$PM_{2.5}$ pollution by the boundary layer structure, we used ERA5 data (such as hourly BLH, temperature data, etc.) with a high spatiotemporal resolution as well. In order to strengthen the robustness of our work, we provided a figure of four SWPs based on ERA5 reanalysis data (Fig. S2), which is highly consistent with NCEP reanalysis data at large scales (Figs. 4 and S2). Additionally, we also furtherly compared the differences between NCEP and ERA5 data. As shown in Fig. S3, the geopotential height of NCEP reanalysis data is significantly positively correlated with that of ERA5 data. Especially in eastern China, the correlation coefficient between the two is greater than 0.96, and all of our classification areas have passed the 99% level of significance test. Overall, the results of this study are robust. We have inquired into the influence of local boundary layer structure on compound pollution events based on the hourly PBL and other meteorological variables of ERA5 data. This has deepened our understanding of the mechanism of the compound pollution events in eastern China during summertime.

Table S1-S2 and captions

Table S1. Thresholds for each pollution level of $PM_{2.5}$ and O_3-8h.

AQI	Pollution level	$PM_{2.5}$(μg m^{-3})	O_3-8h (μg m^{-3})
0~50	Good	0~35	0~100
51~100	Moderate	36~75	101~160
101~150	Lightly polluted	76~115	161~215
151~200	Moderately polluted	116~150	216~265
201~300	Heavily polluted	151~250	266~800

Table S2. The location index of the WPSH under four SWPs.

WPSH	Type 1	Type 2	Type 3	Type 4
The western ridge point	120°E	127.5°E	110°E	95°E
The northern boundary	30°N	32.5°N	37.5°N	40°N
The ridge axis	22°N	25°N	32.5°N	37.5°N

Figures S1-S13 and captions

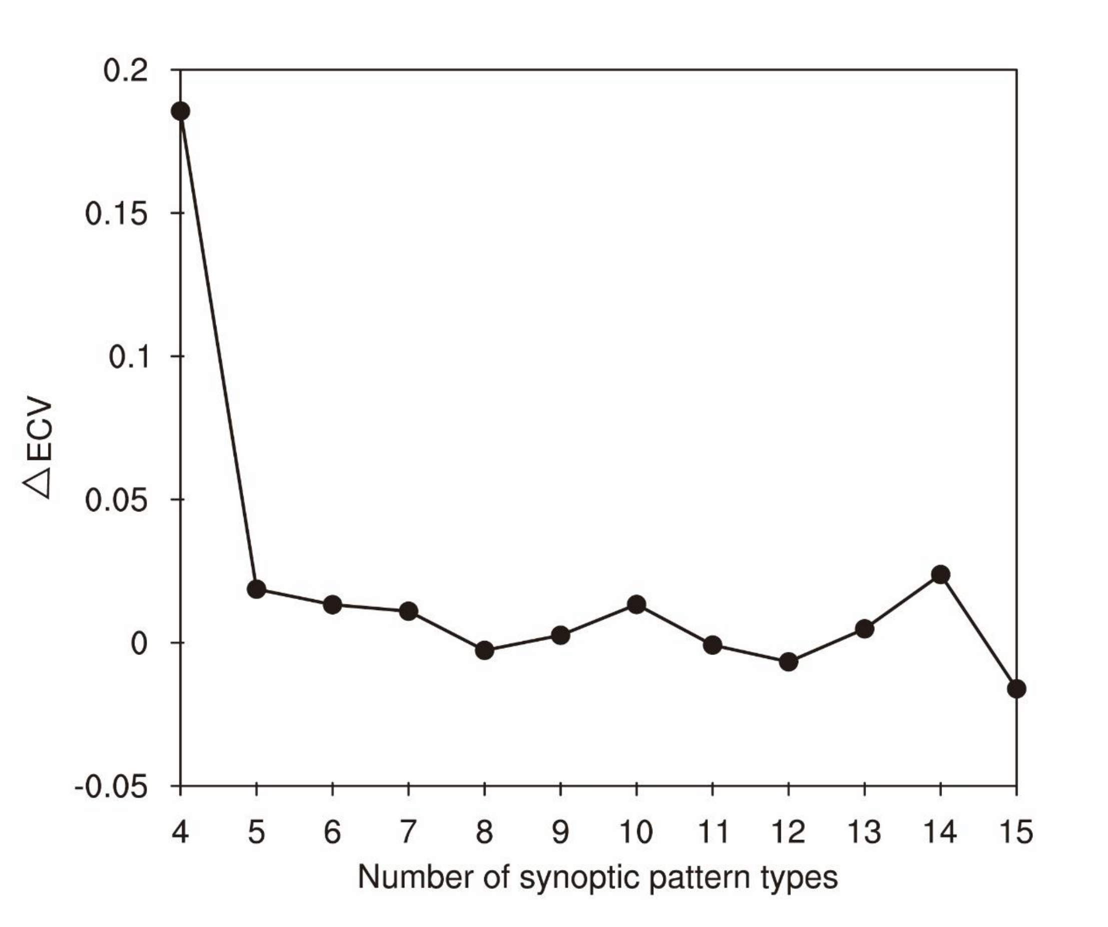

Fig. S1. Changes of *ΔECV* with different numbers of classified synoptic patterns.

85

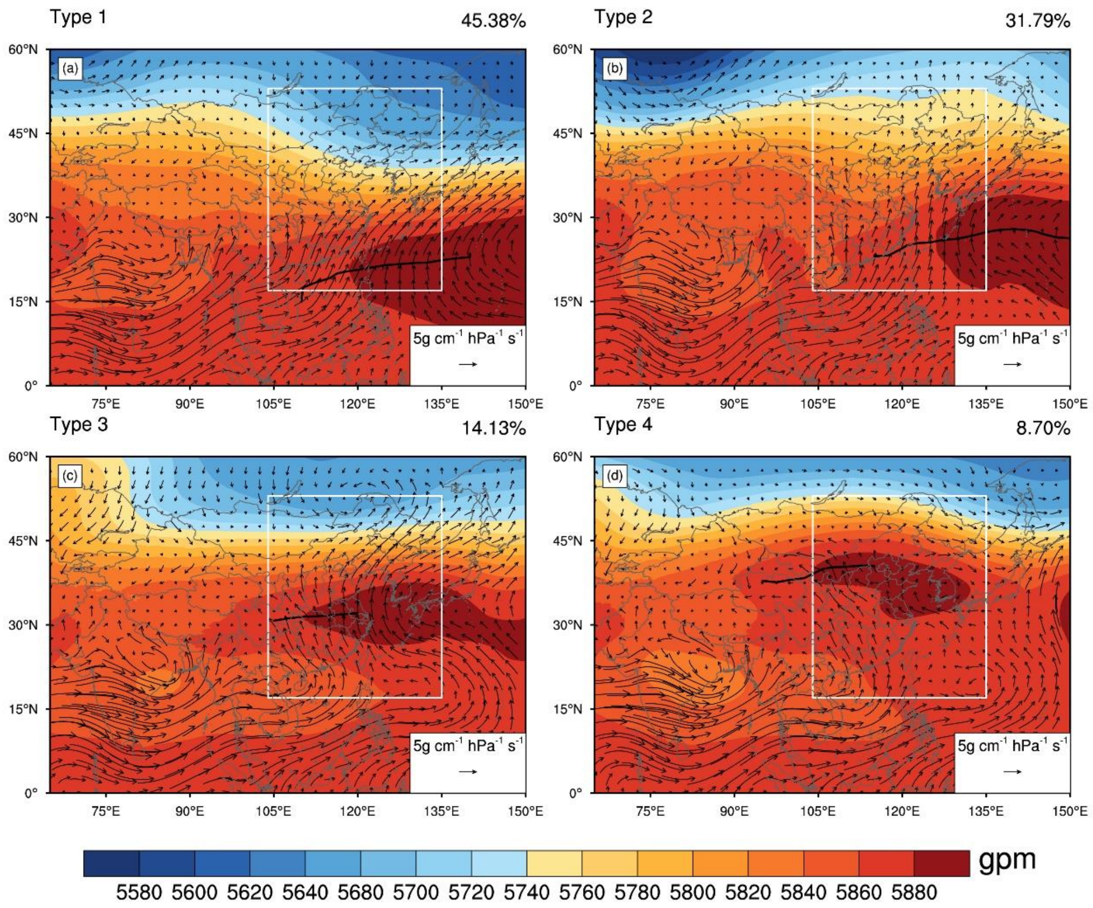

Fig. S2. As in Fig. 4 but for ERA5 reanalysis data.

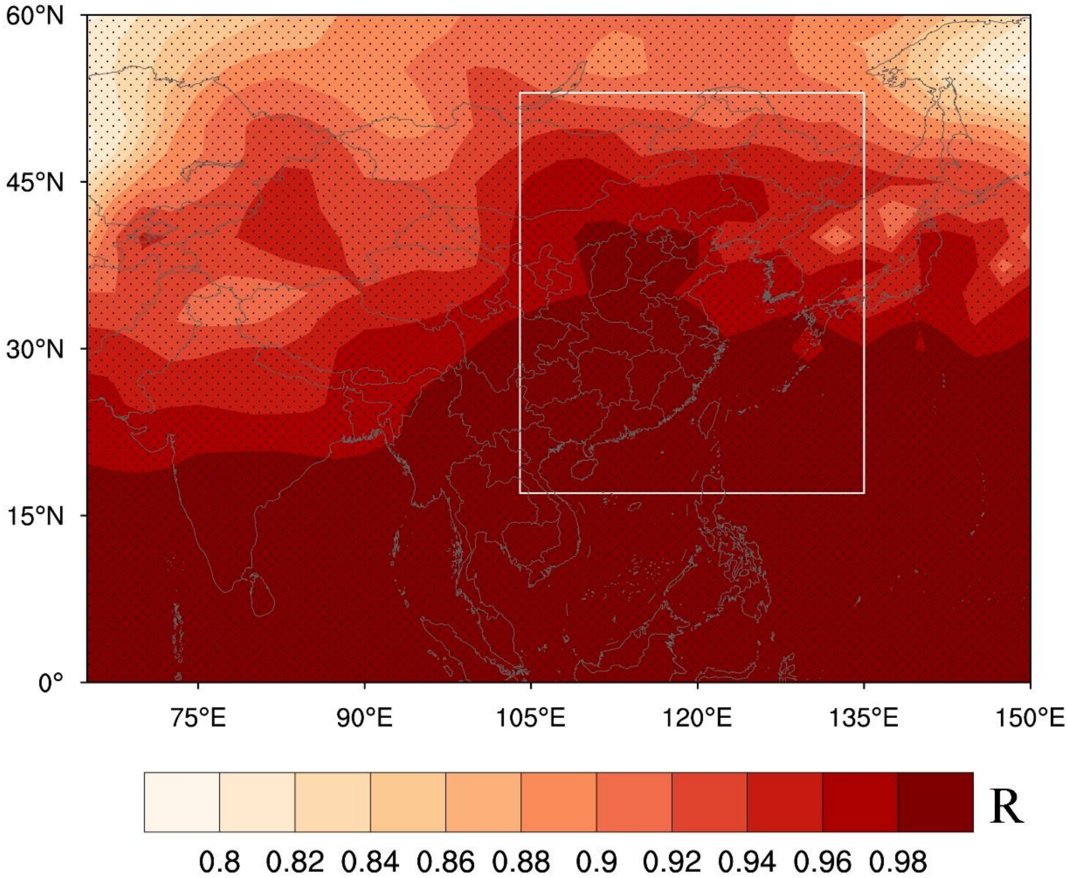

Fig. S3. The correlation of GH between NCEP and ERA5 reanalysis data. The shading indicates the correlation, and the black dots indicate passing the 99% level of significance test.

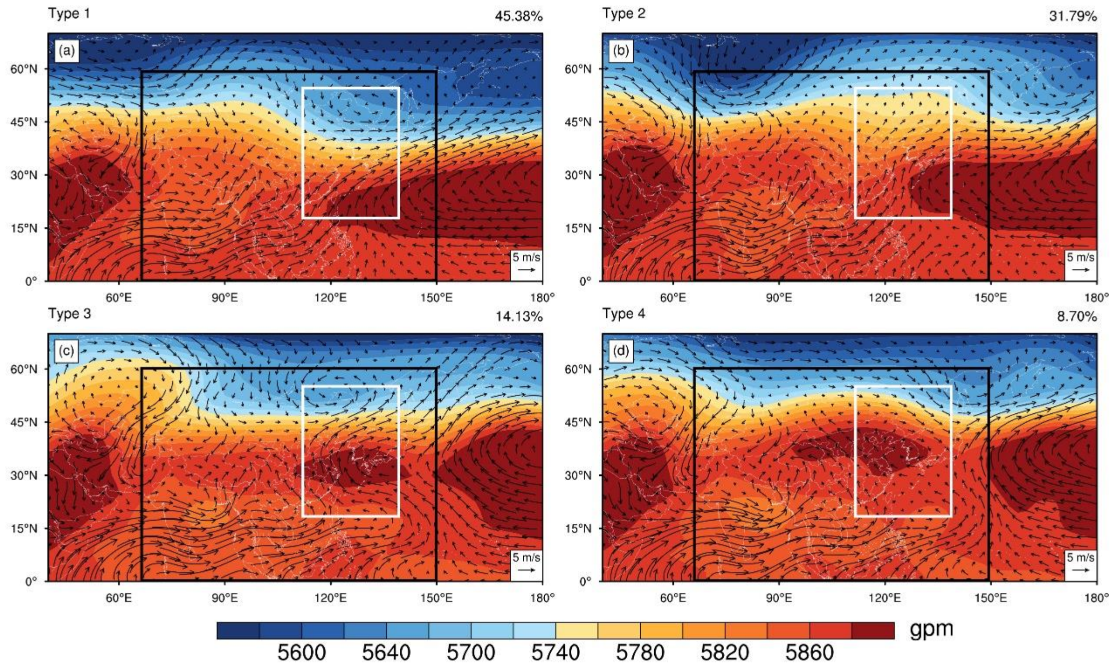

Fig. S4. 850-hPa wind (vectors; see scale arrow at the bottom right in units of 5m/s) and 500-hPa GH (contours; see scale bar at bottom in units of gpm) patterns based on objective classification (see text for details). the black framed area indicates the area for classification and the white framed area for the area of eastern China, the number in the upper-right corner of each panel indicates the frequency of occurrence of each pattern type.

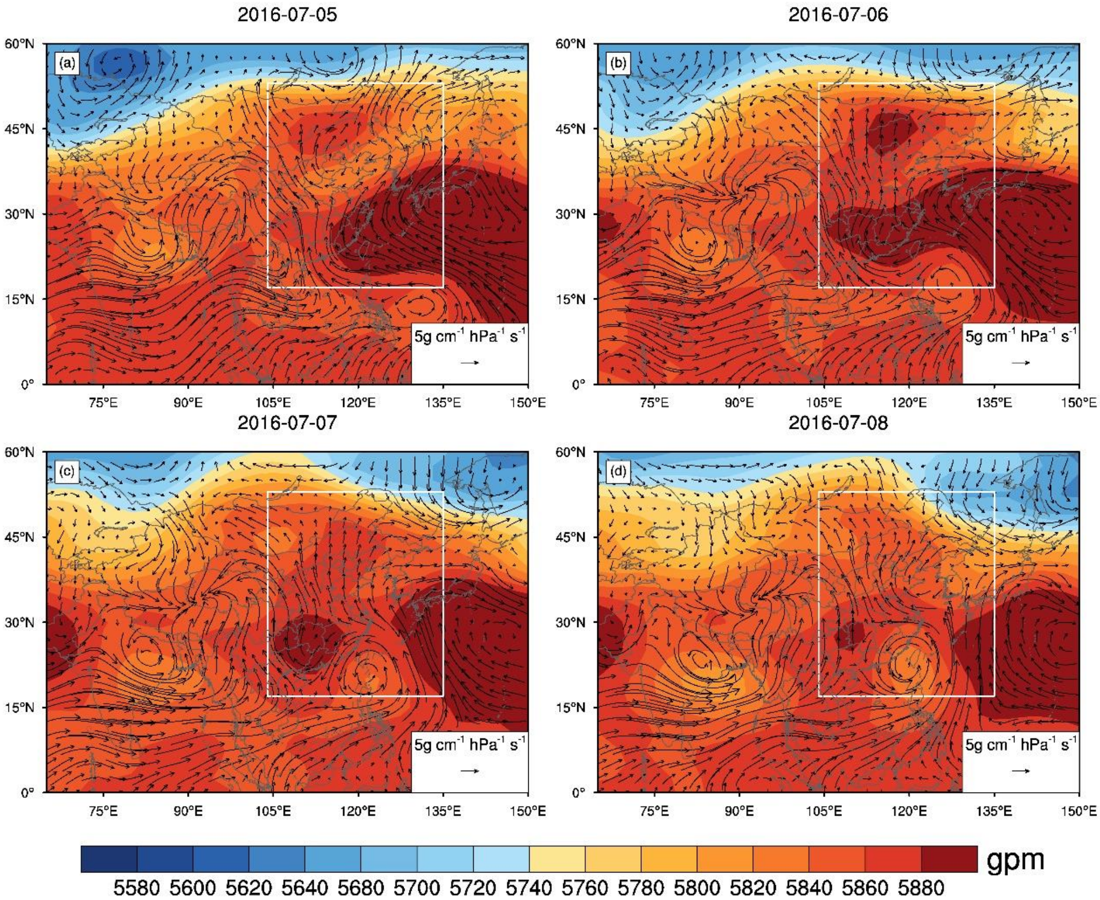

Fig. S5. The SWP case influenced by super typhoon NEPARTAK during July 5-8,2016.

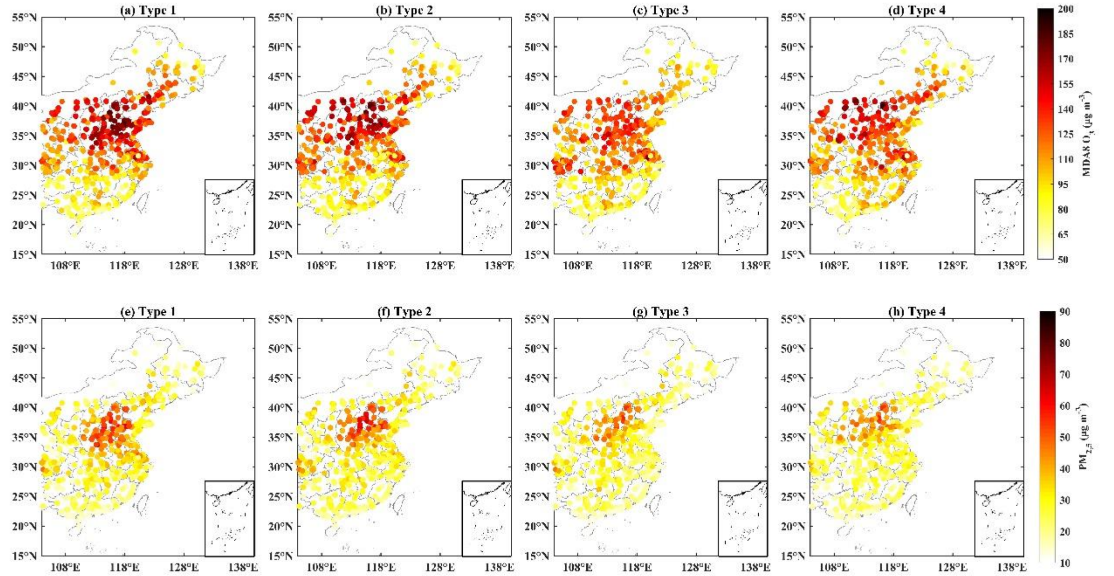

Fig. S6. Average concentrations of MDA8 O_3 and $PM_{2.5}$ under the four SWPs.

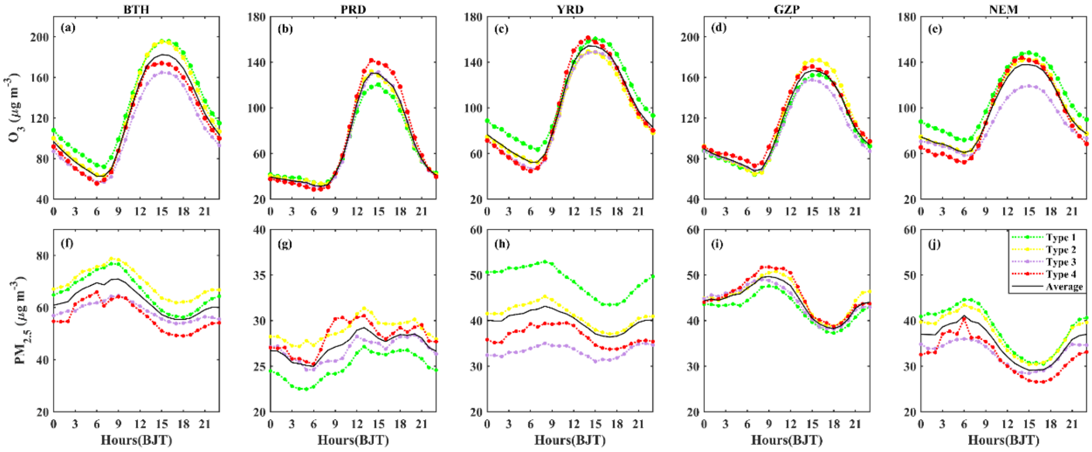

Fig. S7. Daily variations of O_3 and $PM_{2.5}$ under the four SWPs in key urban clusters.

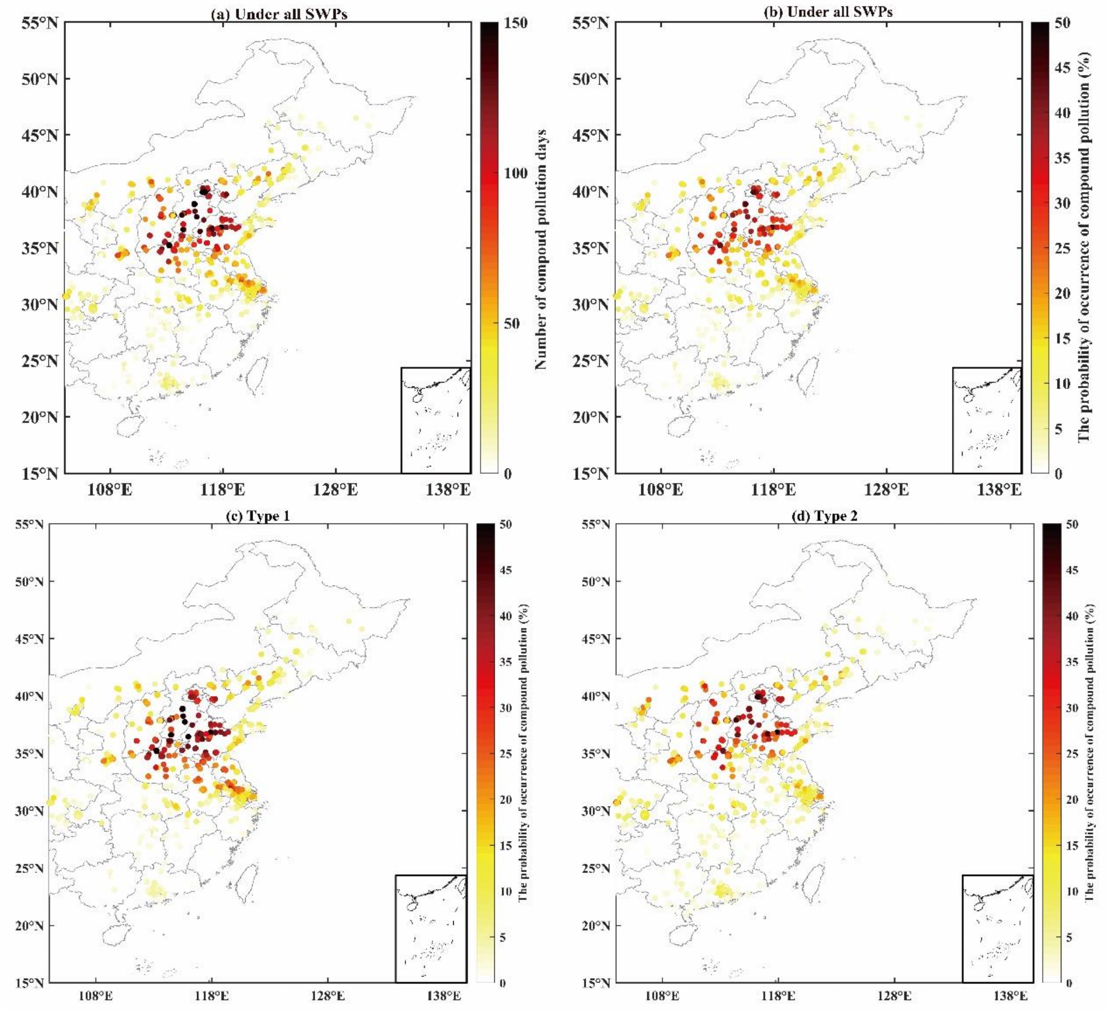

Fig. S8. The number (a) and probability (b) of occurrence of compound pollution days under all SWPs in each site, (c) and (d) is the same as (b), but for Type 1 and Type 2.

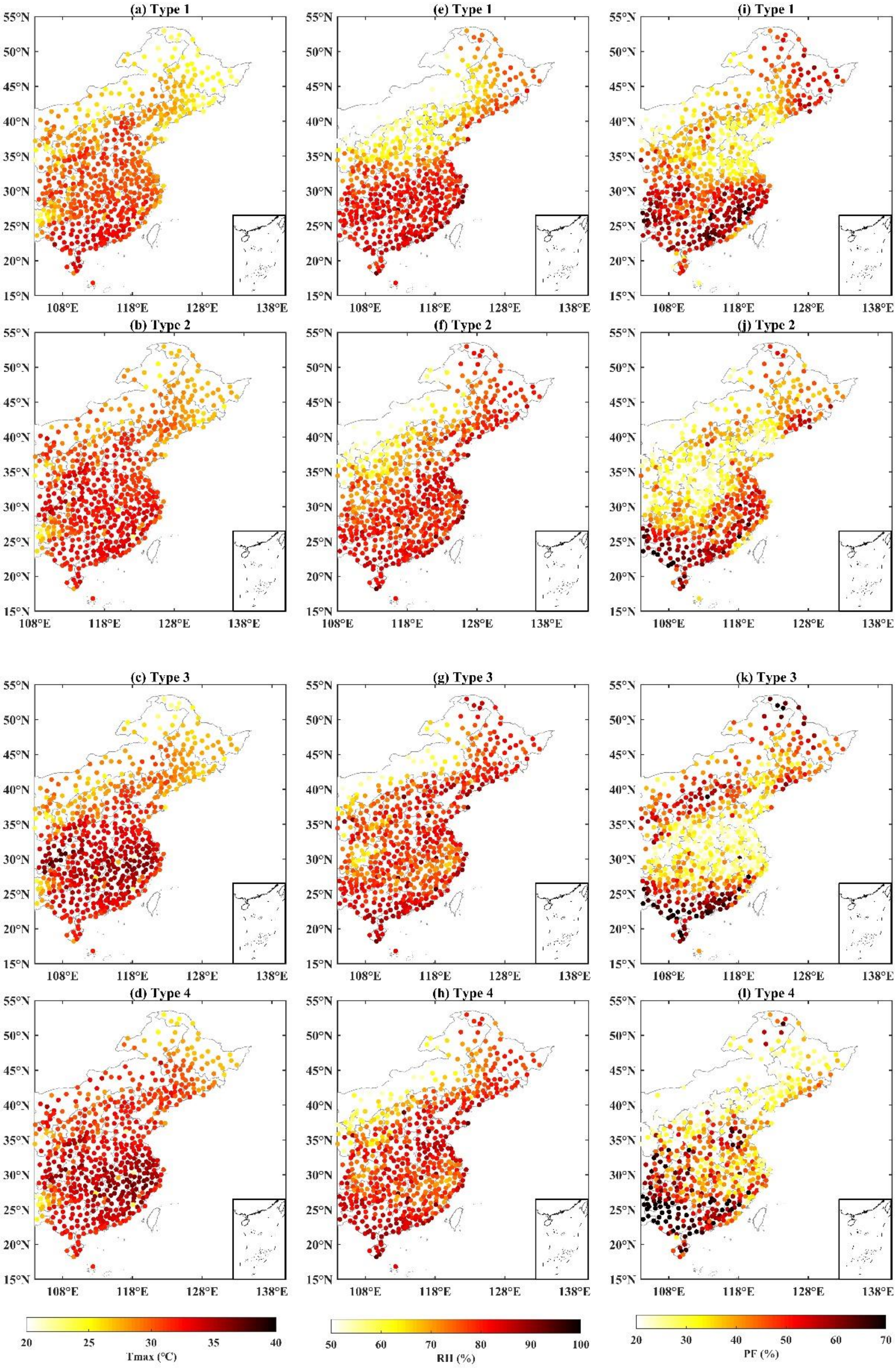

115

Fig. S9. The average of Tmax (a–d), RH (e–h), and PF (i–l) under the four SWPs.

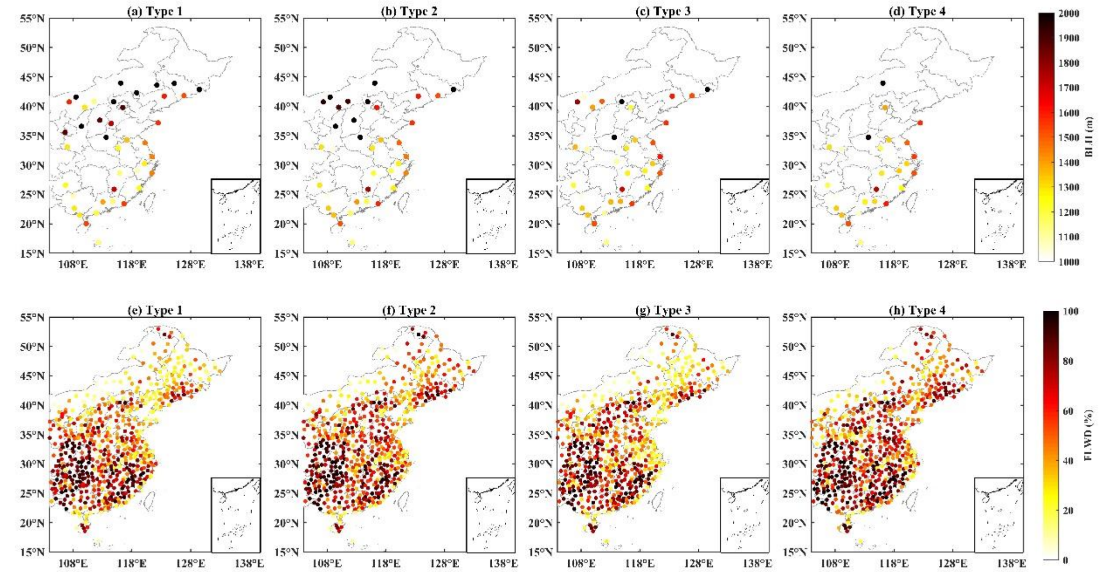

Fig. S10. The average of BLH (14:00) (a–d) and FLWD(e–h) under the four SWPs.

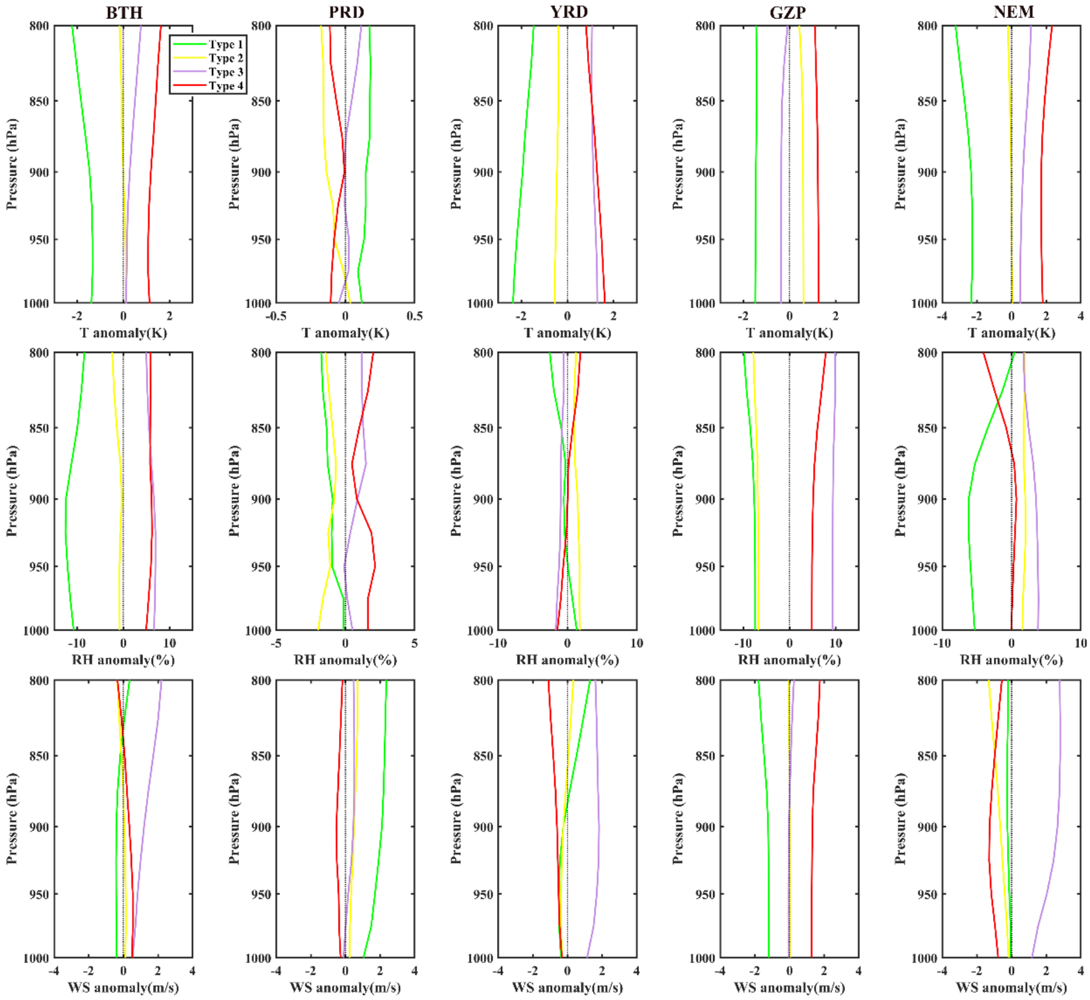

Fig. S11. The vertical profile of temperature, RH, WS (derived from ERA5 reanalysis data) over subregions under each SWP.

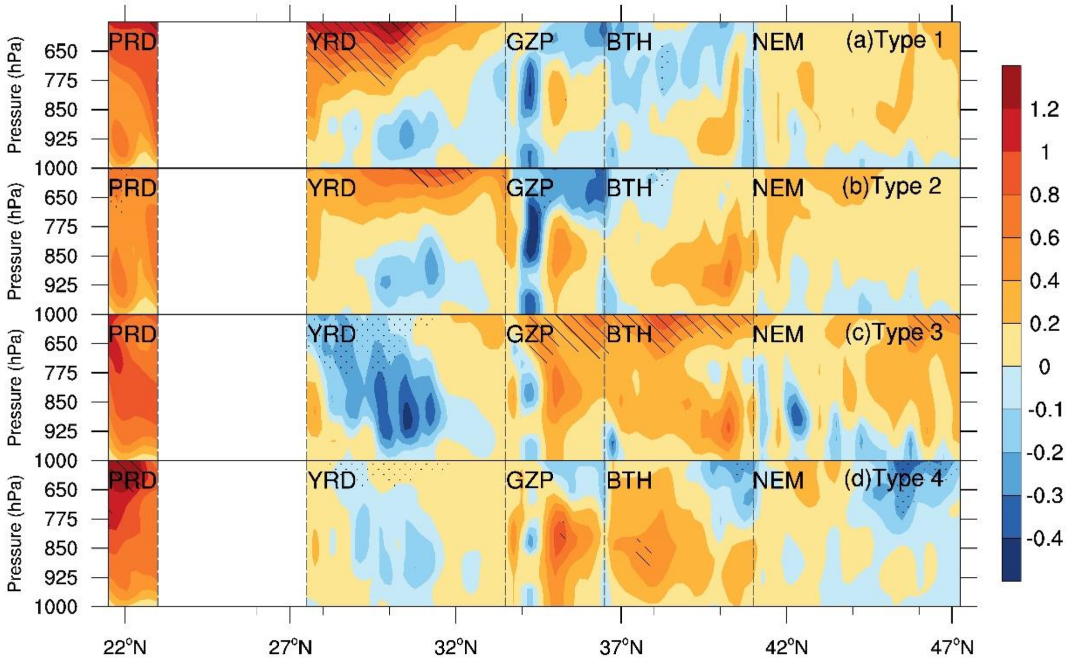

Fig. S12. Vertical cross-sections of the means (shading) and anomalies (filled patterns) of vertical velocity (unit: 10^{-2} m s^{-1}, derived from ERA5 reanalysis data) averaged by longitudes over each region of (a) Type 1, (b) Type 2, (c) Type 3, and (d) Type 4. The dotted and hatched areas represent the negative anomalies less than -3×10^{-2} m s^{-1} and positive anomalies greater than 3×10^{-2} m s^{-1}, respectively. The gray dashed lines indicate the boundaries of PRD, YRD, GZP, BTH and NEM, and the blank area (23°-27.2°N) is not our study region.

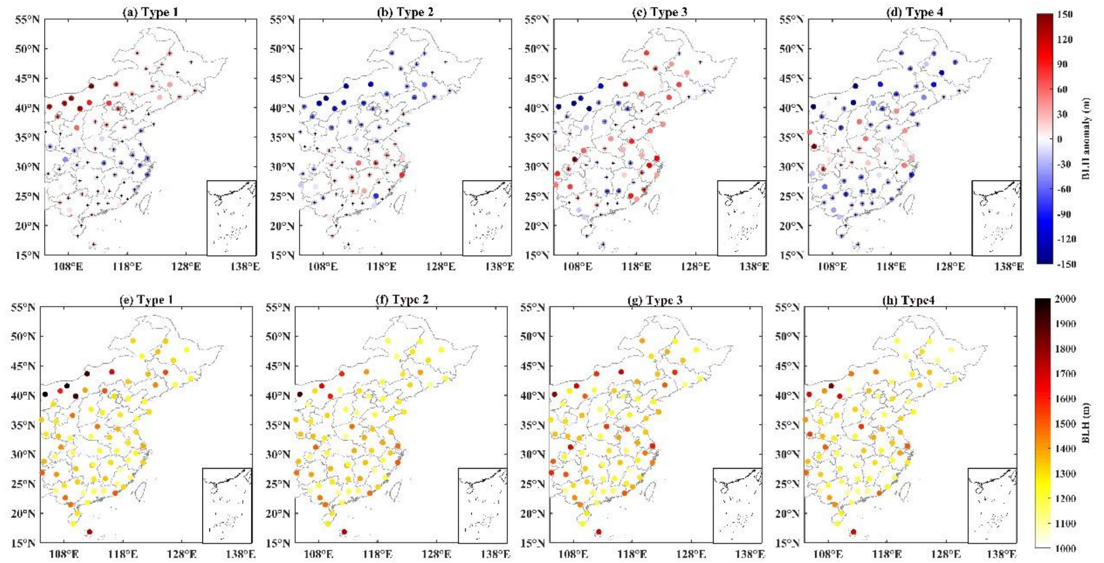

Fig. S13. Average BLHs and their anomalies at 08:00 and 20:00 LT soundings.

135

References

Guo, J., Miao, Y., Zhang, Y., Liu, H., Li, Z., Zhang, W., He, J., Lou, M., Yan, Y., Bian, L. and Zhai, P.: The climatology of planetary boundary layer height in China derived from radiosonde and reanalysis data, Atmos. Chem. Phys., 16(20), 13309–13319, doi:10.5194/acp-16-13309-2016, 2016.

Guo, J., Li, Y., Cohen, J. B., Li, J., Chen, D., Xu, H., Liu, L., Yin, J., Hu, K. and Zhai, P.: Shift in the Temporal Trend of Boundary Layer Height in China Using Long-Term (1979–2016) Radiosonde Data, Geophys. Res. Lett., 46(11), 6080–6089, doi:10.1029/2019GL082666, 2019.

Hoffmann, P. and Heinke SchlüNzen, K.: Weather pattern classification to represent the urban heat island in present and future climate, J. Appl. Meteorol. Climatol., 52(12), 2699–2714, doi:10.1175/JAMC-D-12-065.1, 2013.

Ning, G., Yim, S. H. L., Wang, S., Duan, B., Nie, C., Yang, X., Wang, J. and Shang, K.: Synergistic effects of synoptic weather patterns and topography on air quality: a case of the Sichuan Basin of China, Clim. Dyn., 53(11), 6729–6744, doi:10.1007/s00382-019-04954-3, 2019.

Philipp, A., Beck, C., Esteban, P., Krennert, T., Lochbihler, K., Spyros, P., Pianko-kluczynska, K., Post, P., Alvarez, R., Spekat, A. and Streicher, F.: Cost733 user guide., 2014.

Seidel, D. J., Zhang, Y., Beljaars, A., Golaz, J. C., Jacobson, A. R. and Medeiros, B.: Climatology of the planetary boundary layer over the continental United States and Europe, J. Geophys. Res. Atmos., 117(17), 1–15, doi:10.1029/2012JD018143, 2012.